ARTICLE

Molybdenum Disulfide and Carbon Nanotubes Composite Electrode for Electrochemical Conversion of Salinity Gradient Energy

Jia-Jun Li, Wei-Bin Zhang*, Xin-Yu Liu, Jing-Lei Yang, Yi Yin, Ze-Qin Yang, Xue-Jing Ma*

College of Materials and Chemistry & Chemical Engineering, Chengdu University of Technology, Chengdu 610059, China

Abstract

The ocean accounts for 97% of the total water resources on earth, covering over 70% of the map's surface area. With the continuous consumption of non-renewable energy sources such as fossil fuels and the rapid development of renewable energy, humans are increasingly paying attention to the utilization of ocean resources. Ocean energy includes tidal energy, wave energy, temperature difference energy, and salinity gradient energy. Salinity gradient energy is the energy generated by the interaction of seawater and fresh water, which is the ocean energy existing in the form of chemical energy. This energy is mostly generated in estuaries. The osmotic pressure generated by mixing water with different salinity can be converted into electrical energy driven by potential differences or ion gradients. Salinity gradient energy, as a new renewable energy source, has received widespread global attention and research in recent years, making rapid progress. The utilization of salinity gradient energy provides a renewable and sustainable alternative to the recent surge in global energy consumption.

At present, pressure delay osmosis technology, reverse electrodialysis technology and capacitive mixing technology are three main technologies for extracting salinity gradient energy. In this work, we built a new type of salt difference cell based on capacitive mixing technology, using molybdenum disulfide (MoS_2) and multiwalled carbon nanotubes (MoS_2/MWCNTs) composite electrode as the anode and an activated carbon (AC) as the cathode.

We composited two materials with different ion storage mechanisms together. MoS_2 has a layered structure like graphene, with an interlayer spacing of about twice that of graphene. It is a battery electrode material that can undergo intercalation reaction with Na^+. MWCNTs have a typical double electric layer effect. When discharging, while adsorbing Na^+ on its surface, it can help Na^+ enter the interlayer of MoS_2 more quickly, accelerating the ion transport efficiency and the extraction efficiency of salt differential energy. We conducted physical and electrochemical characterizations of MoS_2/MWCNTs composite material, and tested its salt difference energy extraction ability on a salt difference battery composed of it and AC electrode. We found that the concentration response voltage reached 150 mV, and the energy density of the extracted salt difference energy after a complete four-step cycle reached up to 6.96 $J \cdot g^{-1}$. The advantages of low raw material price of the device and without using ion membranes make it more environmentally friendly, providing a new approach for the study of extracting salinity gradient energy.

Keywords: Salinity gradient energy; Electrochemical conversion; Conversion efficiency; Molybdenum disulfide; Carbon nanotubes

1. Introduction

The salinity gradient energy, generated by the interaction of seawater and river water [1], is a research hotspot in the exploitation and utilization of marine resources, among which the most important are pressure delay osmosis technology, reverse electrodialysis technology and the latest

Received 16 September 2023; Received in revised form 18 September 2023; Accepted 19 September 2023
Available online 25 September 2023

* Corresponding author, Wei-Bin Zhang, Tel: (86-28) 84078940, E-mail address: zhangweibin17@cdut.edu.cn.
* Corresponding author, Xue-Jing Ma, Tel: (86-28) 84078940, E-mail address: maxuejing17@cdut.edu.cn.

https://doi.org/10.13208/j.electrochem.2307121

capacitance mixing technology. Pressure delayed infiltration technology relies on a semi permeable membrane to move water molecules from low concentration to high concentration, causing the volume of the solution on the high concentration side to expand and generate electricity by pushing a water turbine [2−10]. The reverse electrodialysis technology relies on the anion/cation membrane to separate the concentrated solution from the dilute solution, form an ion flow on the inside, and then form a circuit through the external resistance to form a current [11−19]. These two technologies focus on membranes and their main problems are easy fouling, high cost, and difficulty in commercialization [20]. Z. Shan et al. used mesoporous carbon silicon anodized aluminum oxide (MCS/AAO) nanofluid devices and studied using reverse electrodialysis technology to obtain higher performance by adjusting temperature and pH [21]. They also constructed mesoporous carbon titanium dioxide/anodized aluminum oxide hetero-channels (MCT/AAO) with dual functions of cation selectivity and light response. Theoretical and experimental results indicate that excellent photogenerated potential is responsible for bi-directional adjustable ion transport. Therefore, MCT/AAO has the function of collecting ion energy from equilibrium electrolyte solutions, greatly expanding its practical application fields [22].

Capacitive mixing technology [23−25] takes an electrode as the core, including electrochemical double layer capacitance mixing technology, membrane capacitance mixing technology and entropy of mixing battery [26]. The electrode of the double layer hybrid technology is a double layer pseudocapacitive material that can adsorb the anions and cations in the solution onto the surfaces of both electrodes [27−29]. In 2009, D. Brogioli firstly proposed the dual layer capacitive hybrid technology, using commercial activated carbon as the symmetrical electrode [30]. Then S. Ahualli et al. used 0.02 $mol \cdot L^{-1}$ sodium chloride solution at 75 °C and 0.5 $mol \cdot L^{-1}$ sodium chloride solution at 25 °C as electrolytes, and achieved an average power density of 40 $mW \cdot m^{-2}$ after four steps of cycling [31]. The membrane capacitor hybrid technology involves adding anion and cation membranes on the surface of the electrodes. After passing through the membrane, the two electrodes are charged in the opposite direction, resulting in a high concentration response voltage without external power supply [32]. Fei Liu et al. achieved a maximum electrical energy of about 76 $J \cdot m^{-2}$ and an average power density of about 205 $mW \cdot m^{-2}$ by introducing an external power source into the system [33]. The entropy of mixing battery is also called battery mixing technology, which is different from double layer capacitance mixing technology and membrane capacitance mixing technology. It uses electrode materials that can oxidize/reduce with ions in solution or insert/deinsert [34]. M. Ye et al. used $Na_4Mn_9O_{18}$//Ag/AgCl battery to extract salt differential energy in 0.32 $mol \cdot L^{-1}$ of sewage and 0.6 $mol \cdot L^{-1}$ of seawater, which can generate 0.44 $kW \cdot h$ of power per 1 m^3 of sewage. However, the Ag/AgCl electrode in the battery suffers from Ag depletion [35,36].

Z. Shan et al. constructed a multi-layer asymmetric mesoporous carbon/anodic alumina/mesoporous silica (MC/AAO/MS) nanofluid device with rich ordered mesoporous channels using a super assembly strategy. MC/AAO/MS couples the MC and MS dual-ion selective layers, which ensures a high ionic conductance and evidently enhances the cation selectivity [37]. Molybdenum disulfide (MoS_2) is a battery type material, which can insert/deinsert with Na^+ [38,39]. As shown in Fig. 1, it is tightly packed with three layers of S−Mo−S covalent bonds separated by van der Waals gaps, forming channels between the layers that allow Na^+ to undergo insert/deinsert reactions in layers [40]. On this basis, we introduce multiwalled carbon nanotubes (MWCNTs) and composite with MoS_2. The MWCNTs have a typical double electric layer effect. When discharging, while adsorbing Na^+ on their surface, it can help Na^+ enter the

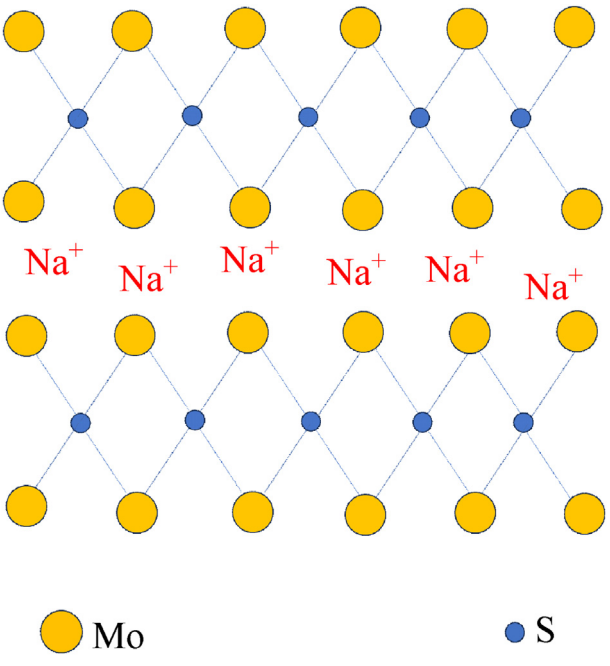

Fig. 1. Schematics of MoS_2 and Na^+ insertion method diagram.

interlayer of MoS_2 more quickly, accelerating the ion transport efficiency and the extraction efficiency of salt differential energy. The MWCNTs are excellent electrode materials for salt difference capacitors because of their high electrochemistry, good stability, conductivity, strong mechanical properties, large active surface area and typical electric double layer effect [41].

Herein, we used a composite material of MoS_2/MWCNTs as the anode and an activated carbon (AC) as the cathode to construct a new type of salt difference cell, and studied the various phase properties of MoS_2/MWCNTs composite materials with different mass ratios. We prepared 0.0086 $mol \cdot L^{-1}$ NaCl solution to simulate fresh water and 0.6 $mol \cdot L^{-1}$ NaCl solution to simulate seawater. In this system, the double layers of MWCNTs and MoS_2 have a synergistic effect. The MWCNTs can better insert/remove Na^+ between the layers of the MoS_2. After a complete four-step cycle, the maximum extracted energy density could reach 6.96 $J \cdot g^{-1}$ or 55.68 $mJ \cdot cm^{-2}$, which is a 13.7% increase compared to previous work result of 6.12 $J \cdot g^{-1}$ [42].

This work combines two materials with different ion storage mechanisms, demonstrating good performance in the field of extracting salinity gradient energy and potential application value in this field. The raw material price of the device is low, and it does not use ion membranes, making it more environmentally friendly, providing a new approach for the study of extracting salinity gradient energy.

2. Experimental Section

For the synthesis of MoS_2/MWCNTs or pure MoS_2, $Na_2MoO_4 \cdot 2H_2O$ (Chengdu Jinshan Chemical Reagent Co., Ltd., China), H_2NCSNH_2 (Chengdu Jinshan Chemical Reagent Co., Ltd., China) and MWCNTs (Jiangsu Xianfeng Nano Material Technology Co., Ltd., China) were used. Thiourea ($CS(NH_2)$) was used as the sulfur source and sodium molybdate (Na_2MoO_4) was used as the molybdenum source in this study. After being weighed according to the stoichiometric ratio, it was added into the beaker. The reaction is given below.

$$4Na_2MoO_4 + 15CS(NH_2) + 6H_2O \rightarrow 4MoS_2 + Na_2SO_4 + 6NaSCN + 24NH_3 + 9CO_2 \quad (1)$$

An appropriate amount of MWCNTs was added, so that the mass ratios of MoS_2 in the products were 45:1, 45:2, 45:3, 45:4, and 45:5 according to the MoS_2: MWCNTs. After ultrasonic treatment of the mixed solution for 10 minutes, it was transferred to a polytetrafluoroethylene lining. The lining was then placed in a reaction kettle and heated at 200 °C for 24 h. The resulting black product was washed three times with deionized water and ethanol, and then placed in an oven and dried at 30 °C to obtain black powder. A composite of MoS_2 and MWCNTs, 8 mg of the as-prepared MoS_2/MWCNTs, was used according to the mass ratio of active substance: acetylene black: polyvinylidene tetrafluoroethylene = 8:1:1 to configurate slurry, and evenly coated on 1 cm × 1 cm graphite paper, then dried for 30 min in an oven. After drying, the composite powder was placed on a tablet press, and pressed for 12 s under 3 MPa pressure to get an electrode.

The diffraction patterns of the sample were obtained by using powder X-ray diffraction. By analyzing the diffraction patterns and comparing the diffraction data with the standard phases, the composition of the material and the existing substances can be determined. The instrument used was panalytical electromagnetic diffractometer, with the diffraction target Cu K_α (λ = 0.154 nm), and the working power of 45 kV × 40 mA, scanning from 5° to 80°. The synthesized sample was tested by scanning electron microscope. The morphology and microstructure were characterized by scanning electron microscope (Zeiss Supra 55) and transmission electron microscope (FEI Tecnai F20). The elemental composition and elemental distribution were analyzed by energy spectrum point scan and energy spectrum surface scan (mapping). XPS test was carried out with Thermo Scientific K_α X-ray photoelectron spectrometer produced in the United States. The constant analyzer energy (CAE) was used to measure the element composition and element distribution of the sample with the passing energy of 150 eV, and the energy step size of 1 eV. The full-automatic specific surface area and porosity analyzer was used to carry out nitrogen absorption-destruction tests through the Branauer-Emmett-Teller method (BET) with micromeritics ASAP 2460.

Fig. 2(a) is the photographs showing the as-assembled and finished device, while Fig. 2(b) is the detailed information for the disassembled device. In the middle there are two titanium plates, and the electrode plates are respectively fixed on the two titanium plates, and separated by a diaphragm. The shell is composed of two pieces of organic glass, and there are hollow holes on the shell, with one side being the water inlet and the other side being the water outlet. A multimeter was employed to record the voltage change between the two electrodes.

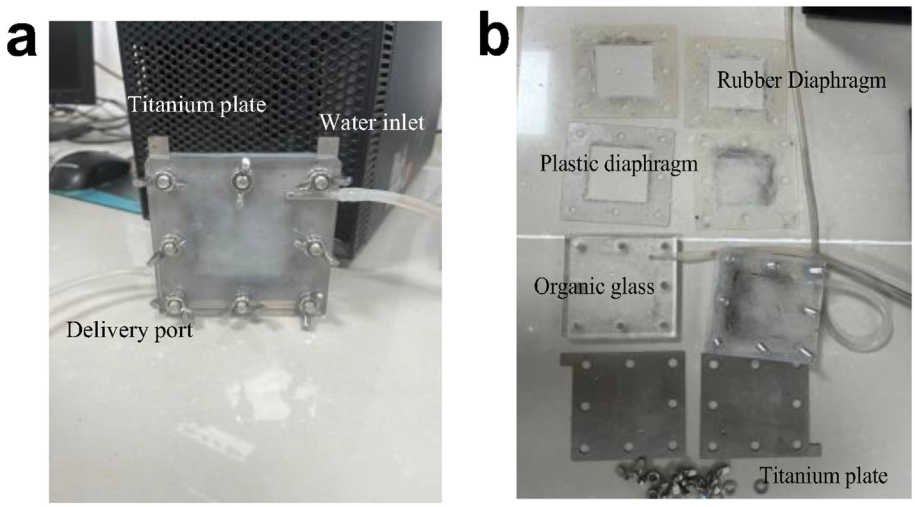

Fig. 2. Photographs showing the device used for collecting salt differential energy. (a) The as-assembled device; (b) the disassmbled device.

3. Results and discussion

3.1. Microstructure and chemical composition

Fig. 3 shows the XRD patterns of the MWCNTs (Curve 1), pure MoS_2 (Curve 2), and MoS_2/MWCNTs composites prepared with different mass ratios of 45:1, 45:2, 45:3, 45:4 and 45:5 (Curves 3−7). Compared to the pure MoS_2 sample, an additional diffraction peak appeared at 26° in the MoS_2/MWCNTs composite materials, with an interlayer spacing of 0.34 nm, corresponding to the (002) crystal plane of MWCNTs [43].

The elemental composition and chemical state of MoS_2/MWCNTs nanocomposites were analyzed using XPS technology. Fig. 4 (a, e, i, m) show the XPS survey spectra of MoS_2/WMCNTs nanocomposites, indicating that the peaks of O1s, $Mo3p_{1/2}$, $Mo3p_{3/2}$, C1s, S2p, Mo4s and Mo4p are presented at 531.4, 412.3, 394.9, 285.1, 163.1, 64.08, and 36.6 eV, respectively. In Fig. 4 (b, f, j, n), the high-resolution XPS spectra of Mo $3d_{5/2}$ and Mo $3d_{3/2}$ reveal two peaks at the binding energies of 228.9 eV and 232.0 eV, which are consistent with the +4 oxidation state of Mo. Near the characteristic peak of Mo 3d, the peak at 226 eV is attributed to S 2s, while the weak peak at around 235 eV is attributed to Mo oxidation. The high-resolution spectra of S 2p in Fig. 4 (c, g, k, o) show that there are two peaks at 161.8 eV and 162.8 eV for S $2p_{3/2}$ of S^{2-} and S $2p_{1/2}$ of S^{2-}, respectively. The weak peak of 169.0 eV can be attributed to S^{2-}, indicating that S^{2-} oxidation has occurred to some extent. Considering the atomic ratio of sulfur to molybdenum, the generated nano sulfides may exist in the form of MoS_2 [41,44]. In addition, the peak spacing between Mo $3d_{3/2}$ (232.0 eV) and Mo $3d_{5/2}$ (228.9 eV) is 3.1 eV, which is consistent with MoS_2. The peak spacing of S $2p_{1/2}$ (162.8 eV) and S $2p_{3/2}$ (161.8 eV) is 1 eV, which is consistent with the peak spacing of divalent sulfur ions (S^{2-}). Fig. 4 (d, h, l, p) show high-resolution spectra of C 1s in MoS_2/MWCNTs. The strong peak at 284.8 eV is caused by sp2 hybrid carbon atoms, and the peak at 286.5 eV corresponds to the oxygen-containing functional groups on the surface of carbon nanotubes [44].

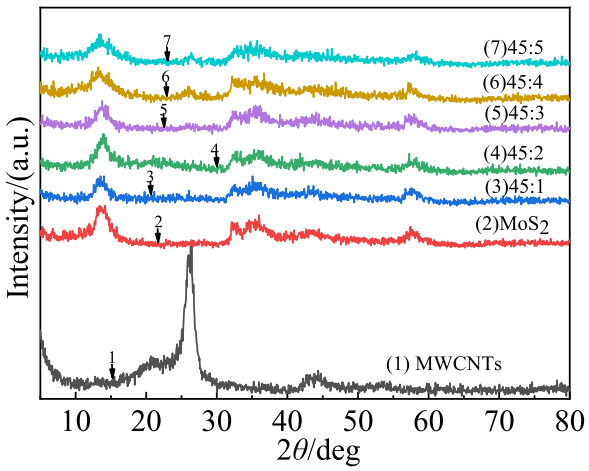

Fig. 3. XRD diffraction patterns of MWCNTs (1), MoS_2 (2) and MoS_2/MWCNTs composite materials prepared with different mass ratios (3−7).

Fig. 5 is the results of MoS_2 (a) and MoS_2/MWCNTs composite materials prepared with the mass ratios ranging from 45:1 to 45:5 (b−f) observed by scanning electron microscope. It can be seen that overall, linear morphologies of MWCNTs are dispersed between MoS_2 nanosheets, and many MoS_2 nanosheets are stacked together to form nanoflowers. A gap is formed between the thin sheets to provide space for the movement of ions. Fig. 6 shows the energy

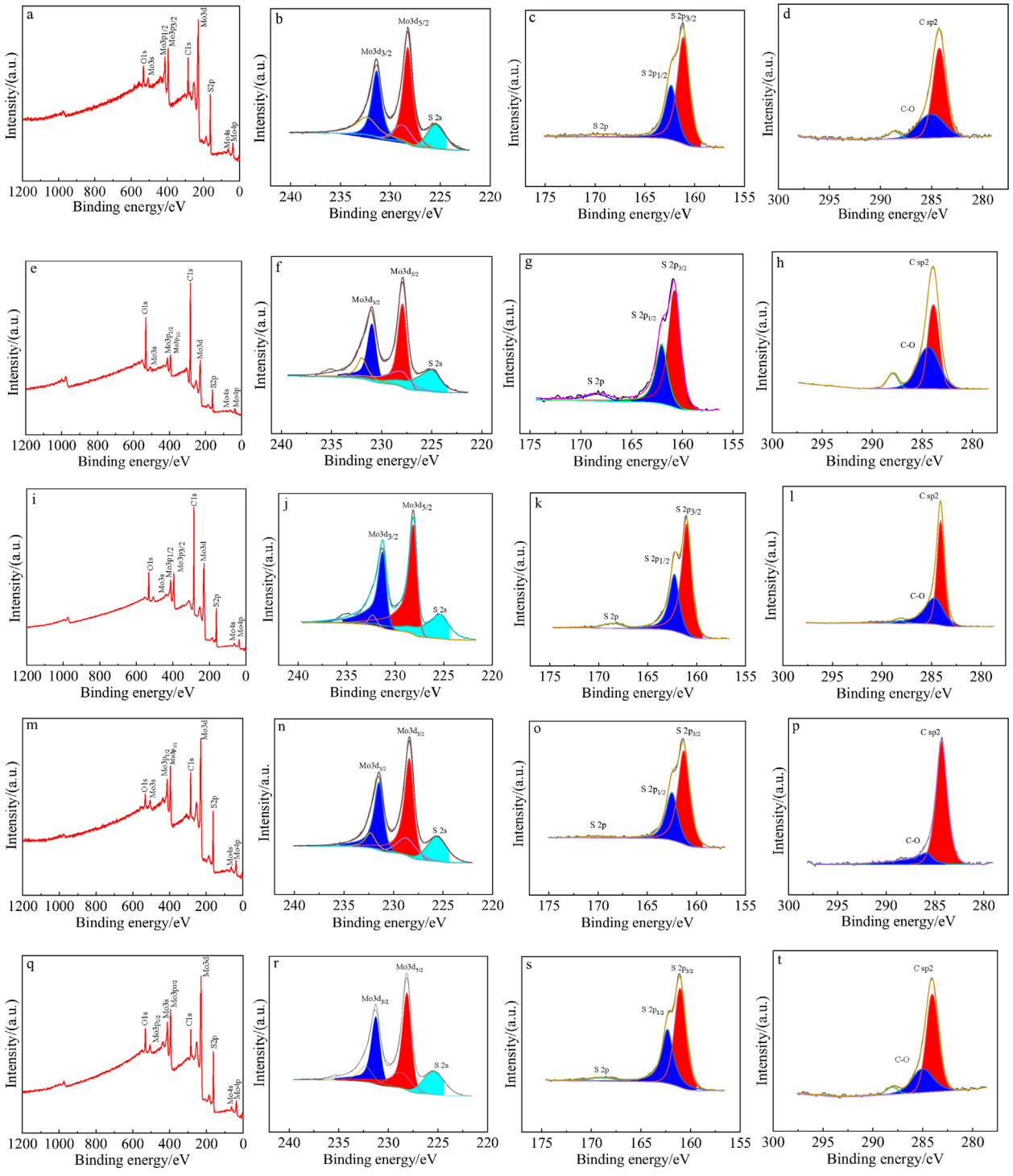

Fig. 4. XPS spectra of MoS_2/MWCNTs composite materials prepared with the mass ratios of MoS_2:MWCNTs varying from 45:1 to 45:5. (a–d) 45:1; (e–h) 45:2; (i–l) 45:3; (m–p) 45:4; (q–t) 45:5.

dispersion spectrum (EDS) of MoS_2/MWCNTs composite materials with different mass ratios, showing the mass and atomic ratios of the elements in the composite material, achieving the expected values.

We also conducted TEM testing on the sample obtained with the mass ratio of 45:4 selected based on the XRD data, and the results are presented in Fig. 7. From Fig. 7(c), the two characteristic lattice stripes are 0.62 nm and 0.34 nm, corresponding to the (002) crystal plane of MoS_2 and the (002) crystal plane of MWCNTs, respectively, confirming that the MoS_2/MWCNTs composite material is successfully synthesized.

Fig. 8 shows nitrogen adsorption/desorption isotherm and the corresponding pore size

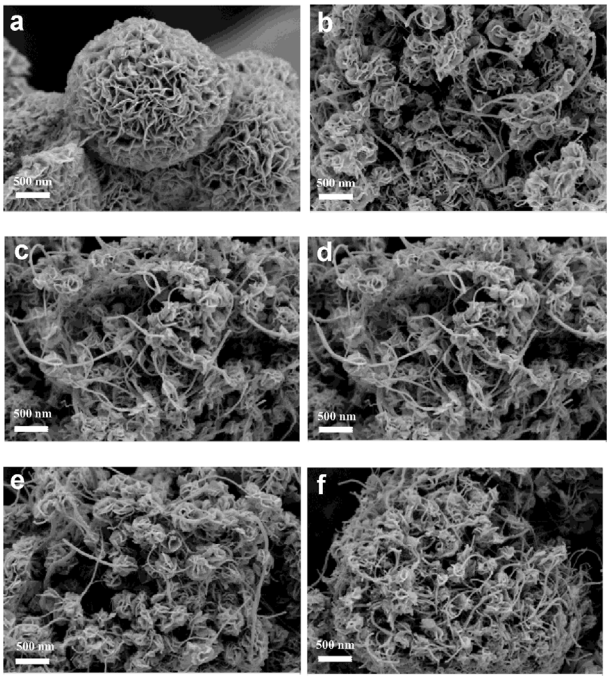

Fig. 5. Scanning electron microscopic images of MoS_2 (a) and MoS_2/MWCNTs composite materials prepared with the mass ratios ranging from 45:1 to 45:5 (b–f). (b) 45:1; (c) 45:2; (d) 45:3; (e) 45:4; (f) 45:5.

distribution curves of MoS_2/MWCNTs composite materials prepared with different mass ratios. It is obvious from Fig. 8 (a, c, e, g, i) that the existence of characteristic hysteresis loop means the nature of mesoporous material. Furthermore, for the mass ratios of 45:1, 45:2, 45:3, 45:4 and 45:5, the BET surface areas of the composite materials are 5.88, 7.34, 12.73, 19.53, and 17.24 $m^2 \cdot g^{-1}$, respectively, while the BJH adsorption cumulative surface areas of pores are 5.25, 7.44, 13.24, 20.30, and 16.83 $m^2 \cdot g^{-1}$, respectively. The BJH destruction cumulative surface areas of pores are 7.30, 12.69, 18.99, 29.10, and 22.99 $m^2 \cdot g^{-1}$, respectively. The average adsorption pore sizes (4 V/a by BET) are 10.02, 9.41, 9.17, 10.28, and 10.54 nm, respectively, while the average desorption pore sizes (4 V/a by BET) are 12.44, 13.63, 12.70, 13.04, and 14.34 nm, respectively. The pore size of mesoporous materials ranges 2~50 nm, which can carry large molecules and facilitate the insertion/removal of ions.

3.2. Electrochemical characterization

The electrochemical workstation was used to perform electrochemical test on the MoS_2/MWCNTs electrode. A low concentration of 0.0086 $mol \cdot L^{-1}$ and a high concentration of 0.6 $mol \cdot L^{-1}$ NaCl solutions were used as the electrolyte. Cyclic voltammetric (CV) test was performed in the potential window of −1 V–0.4 V by varying the scanning rate of 5 $mV \cdot s^{-1}$~100 $mV \cdot s^{-1}$, and the reference electrode was silver chloride electrode. Fig. 9 shows the CV plots of MoS_2/MWCNTs composites prepared with different

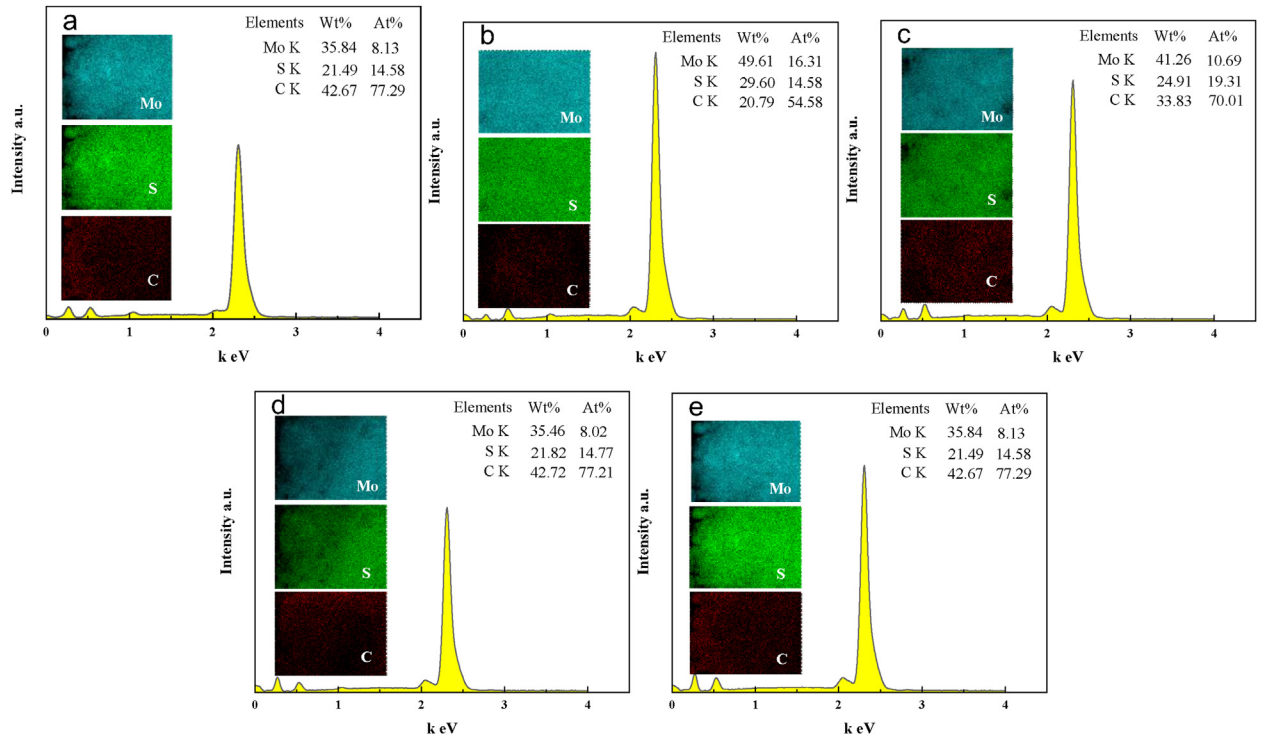

Fig. 6. Energy dispersive X-ray spectroscopic data of MoS_2/MWCNTs composite materials prepared with different mass ratios of MoS_2:MWCNTs. (a) 45:1; (b) 45:2; (c) 45:3; (d) 45:4; (e) 45:5.

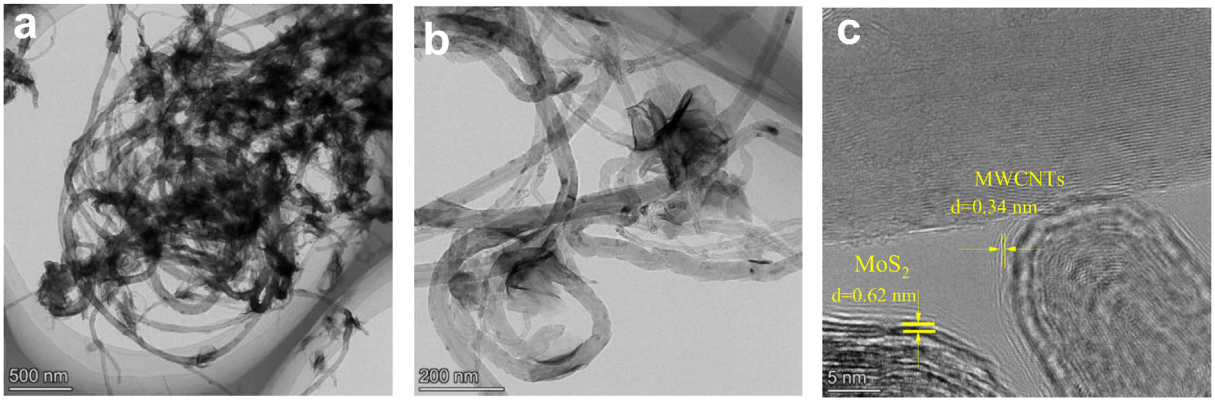

Fig. 7. Transmission electron microscopic images of MoS_2/MWCNTs = 45:4 at (a) 40,000 times magnification; (b) 100,000 times magnification; (c) 4,000,000 times magnification.

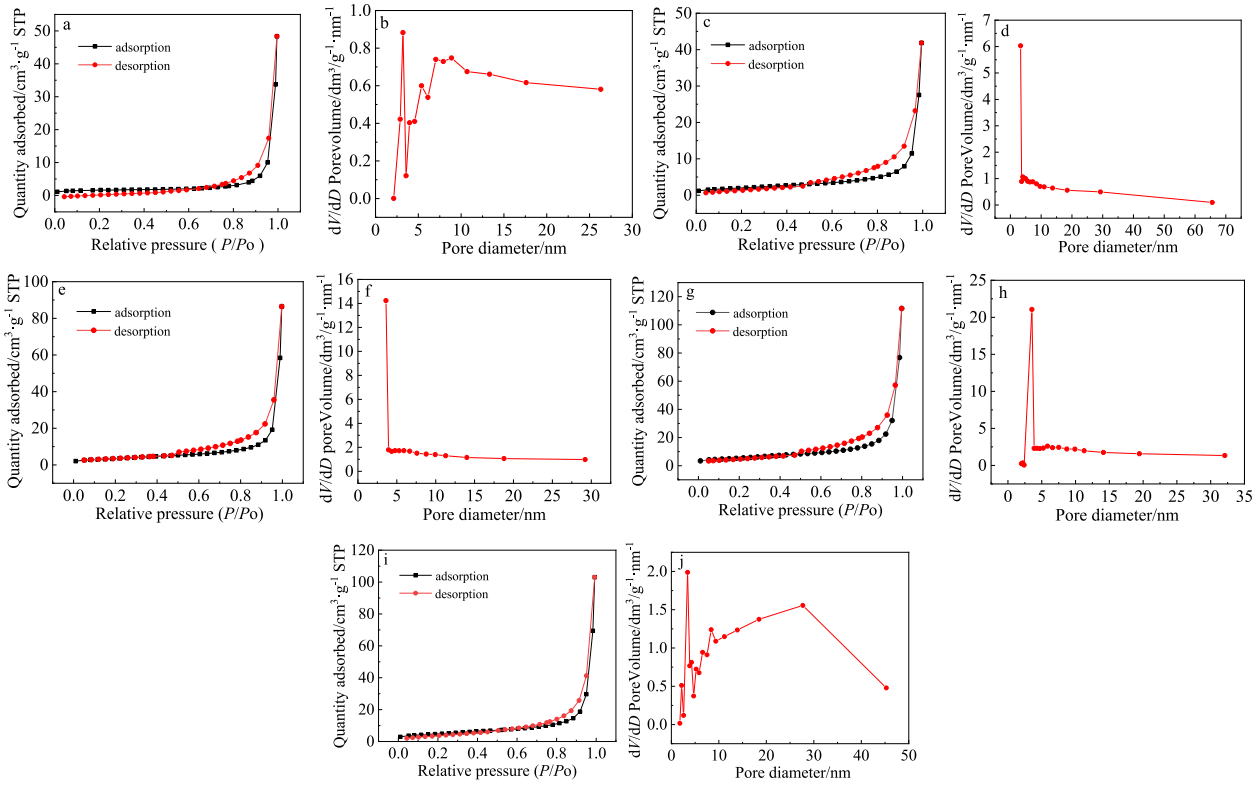

Fig. 8. Nitrogen adsoption/desorption isotherm (a, c, e, g and i) and the corresponding pore size distribution curves (b, d, f, h and j) of the MoS_2/MWCNTs prepared with different mass ratios.

mass ratios. The potential window appears quasi rectangular, indicating that the MoS_2 functioned as a pseudo capacitor when working in NaCl solution [45] via the reaction in Eq. (2).

$$MoS_2 + xNa^+ + xe^- = Na_xMoS_2 \quad (2)$$

The area in 0.0086 mol·L^{-1} NaCl solution is smaller than that in a 0.6 mol·L^{-1} NaCl solution, indicating that the electrode material is highly sensitive to ions. A significant reduction peak appears at a potential around 0.5 V at a low scanning speed, during which an intercalation reaction might occur, and Na^+ ions could be embedded into the interlayer of MoS_2, and Na^+ deintercalation might occur throughout the entire flat wide peak, which is consistent with the reported intercalation pseudo capacitance content [46]. Fig. 10 shows constant current charge-discharge curves, with a potential window of −1 V~0.4 V. By varying the mass ratios of 45:1, 45:2, 45:3, 45:4 and 45:5, the current densities tested were 0.5, 0.6, 0.7, 0.8, 0.9, and 1 A·g^{-1}, respectively, while the specific

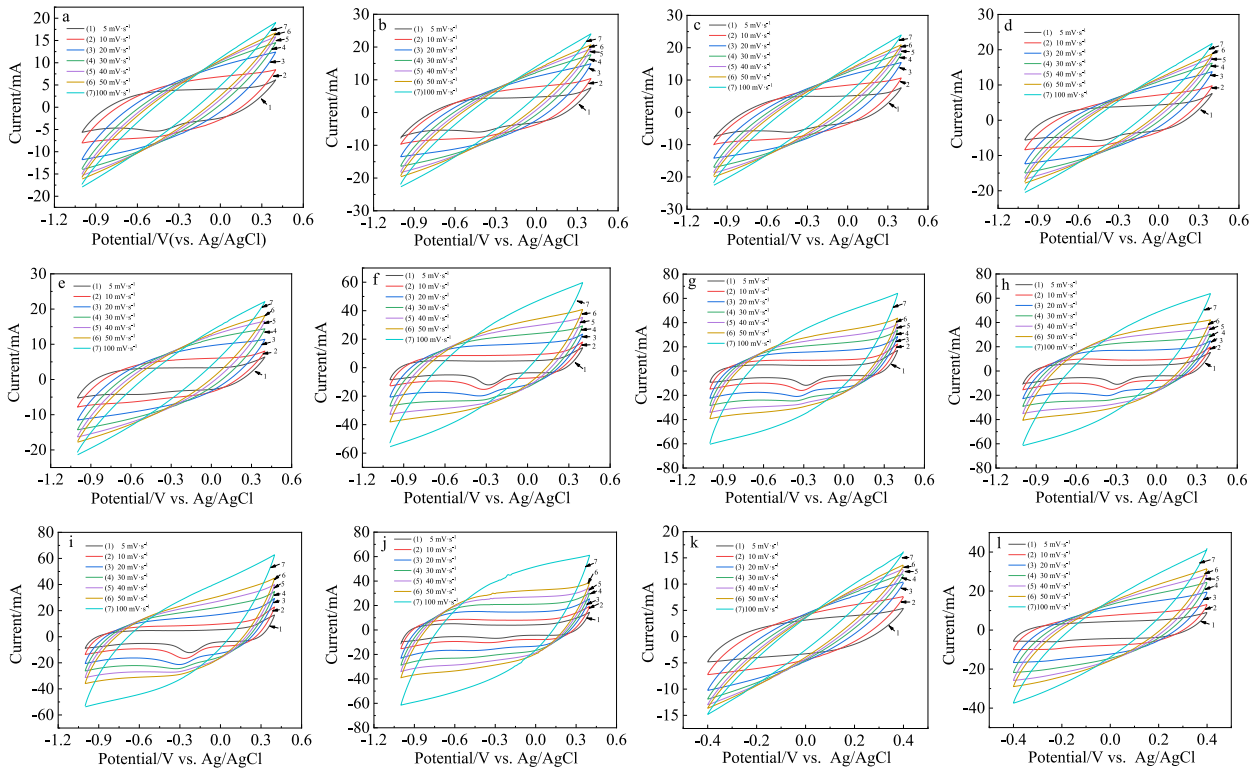

Fig. 9. Cyclic voltammograms of MoS_2/MWCNTs composite materials prepared with different mass ratios. (a—e) 45:1 to 45:5 in 0.0086 mol·L^{-1} NaCl solution; (f—j) 45:1 to 45:5 in 0.6 mol·L^{-1} NaCl solution; Cyclic voltammograms of pure MoS_2 in (k) 0.0086 mol·L^{-1} NaCl solution and (l) 0.6 mol·L^{-1} NaCl solution.

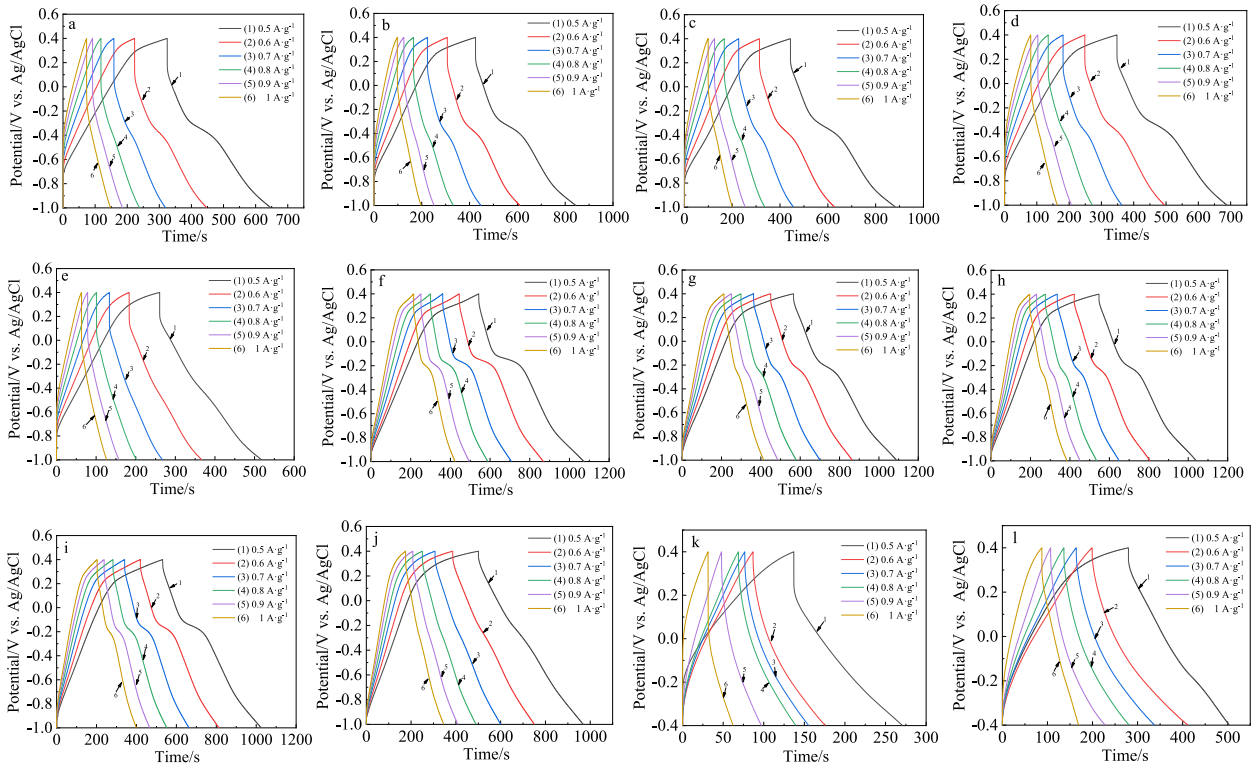

Fig. 10. Galvanostatic charge—discharge (GCD) curves of MoS_2/MWCNTs composite materials prepared with different mass ratios. (a—e) 45:1 to 45:5 in 0.0086 mol·L^{-1} NaCl solution; (f—j) 45:1 to 45:5 in 0.6 mol·L^{-1} NaCl solution; Galvanostatic charge—discharge (GCD) curves of pure MoS_2 in (k) 0.0086 mol·L^{-1} NaCl solution and (l) 0.6 mol·L^{-1} NaCl solution.

capacitance values in 0.6 mol·L^{-1} NaCl solution were 176.4, 186.8, 189.6, 211.8, and 168.2 F·g^{-1}, respectively. Compared to the specific capacitance of pure molybdenum disulfide, accounting for the improvement of 28.4%~61.7%, and a larger specific capacitance indicates that the double layer and ion intercalation/detachment energy interact with more Na^+ ions. Fig. 11(a−e) shows the electrochemical impedance spectra of various MoS_2/MWCNTs composite materials, indicating that the intrinsic impedance and diffusion impedance of MoS_2/MWCNTs electrode in 0.6 mol·L^{-1} NaCl solution are smaller than those in 0.0086 mol·L^{-1} NaCl solution, which is conducive to the

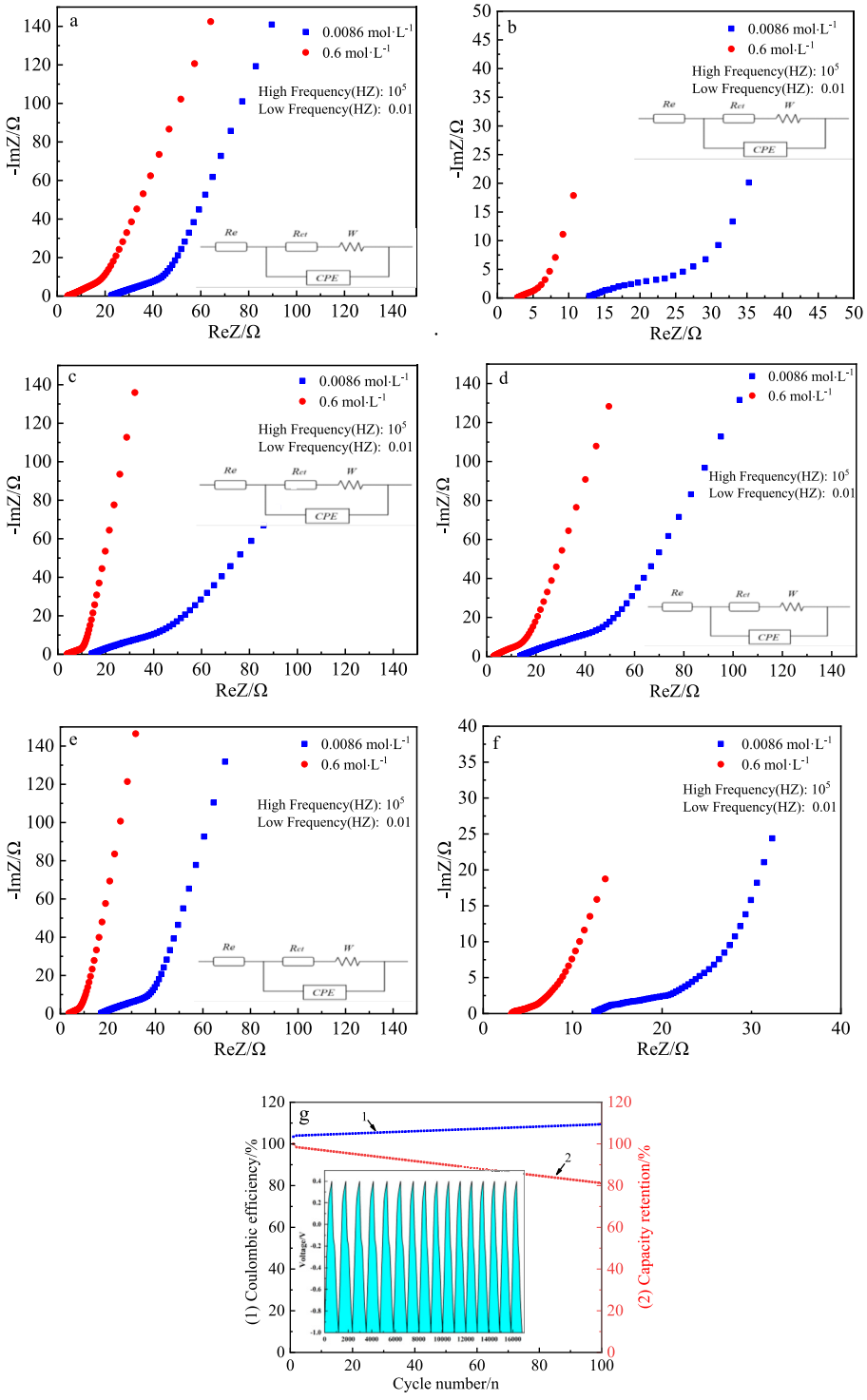

Fig. 11. Electrochemical impedance plots of MoS_2/MWCNTs composite materials prepared with the mass ratio of (a) 45:1; (b) 45:2; (c) 45:3; (d) 45:4; (e) 45:5; (f) EIS plots of pure MoS_2; and (g) 100 cycles of charge and discharge curves for the electrode with a mass ratio of 45:4.

movements of anions and cations in this system. Fig. 11 (g) illustrates the capacity retention rate and charge efficiency of the composite electrode (45:4) with the highest specific capacity after 100 consecutive constant current charges and discharges.

3.3. Extraction of salinity gradient energy

The device as shown in Fig. 2 (a) was assembled and the two electrodes were connected using an electrochemical workstation. The positive electrode was connected to the MoS_2/MWCNTs electrode, and the negative electrode was connected to the activated carbon electrode. We used two pumps to control the delivery of dilute and concentrated solutions, with a flow rate set to 1 $mL \cdot s^{-1}$. The first step was to introduce a dilute solution from one end of the device, and the electrochemical workstation charged the device for 110 seconds. This step is to bring positive and negative charges to the two electrodes separately, allowing the Na^+ ions presented on the surface of the MWCNTs and the MoS_2 layers, at the same time, the Cl^- ions on the activated carbon surface are released into the solution. The second step is to stop charging and introduce a concentrated solution, causing the voltage to be increased. The third step is to apply a reverse current to discharge the device for 110 seconds. During this process, Cl^- ions in the solution will be adsorbed onto the surface of the AC electrode due to the double layer effect. Na^+ ions in the solution is first adsorbed onto the surface of the MoS_2/MWCNTs composite electrode due to the double layer effect, and some Na^+ ions are embedded in the interlayer of MoS_2. Step 4 introduces a dilute solution to cause a voltage drop and restore to its initial state. According to the theory of salt difference energy extraction, the energy generated by the four-step cycle is shown in Fig. 12(a). The area of this graph represents the extracted energy, as the same amount of charge is released at a higher potential, and the resulting energy gain is given based on the integration of voltage and charge [34] according to Eq. (3).

$$W = -\oint \triangle E \, dq \tag{3}$$

Where ΔE is the voltage change in the cycle and q is the amount of charge. The process of charge accumulation in the curve is the first step, the second step, switching the solution, the potential rises, the third step, the device discharges at high potential, and the fourth step, switching the solution, the potential drops.

Fig. 12(b–f) shows the potential difference between the MoS_2/MWCNTs composite electrode and the AC electrode with different mass ratios during the salt difference energy extraction process of the device. It can be seen that the potential increase after switching between fresh water and concentrated salt water are 110, 123, 134, 150, and 113 mV for the different mass ratios.

From this process, the energy density of the salinity gradient that can be extracted by the device after a complete four-step cycle can be obtained. As shown in Fig. 13(d), the highest energy density could reach 6.96 $J \cdot g^{-1}$. Compared with the pure molybdenum disulfide, the extracted energy density has been increased by 13.7%.

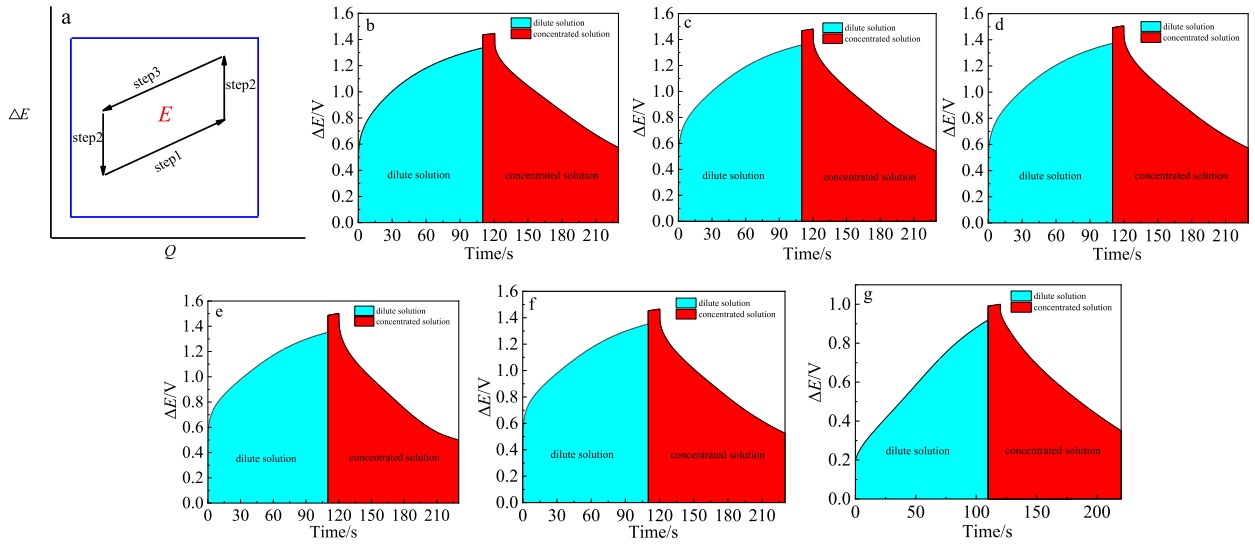

Fig. 12. The principle of generating salinity gradient energy and potential changes during operation. (a) Schematic diagram of extracting salinity gradient energy by device; (b–f) Potential difference between MoS_2/MWCNTs composite electrode and AC electrode with the mass ratio from 45:1 to 45:5; (g) Potential difference between pure MoS_2 electrode and AC electrode.

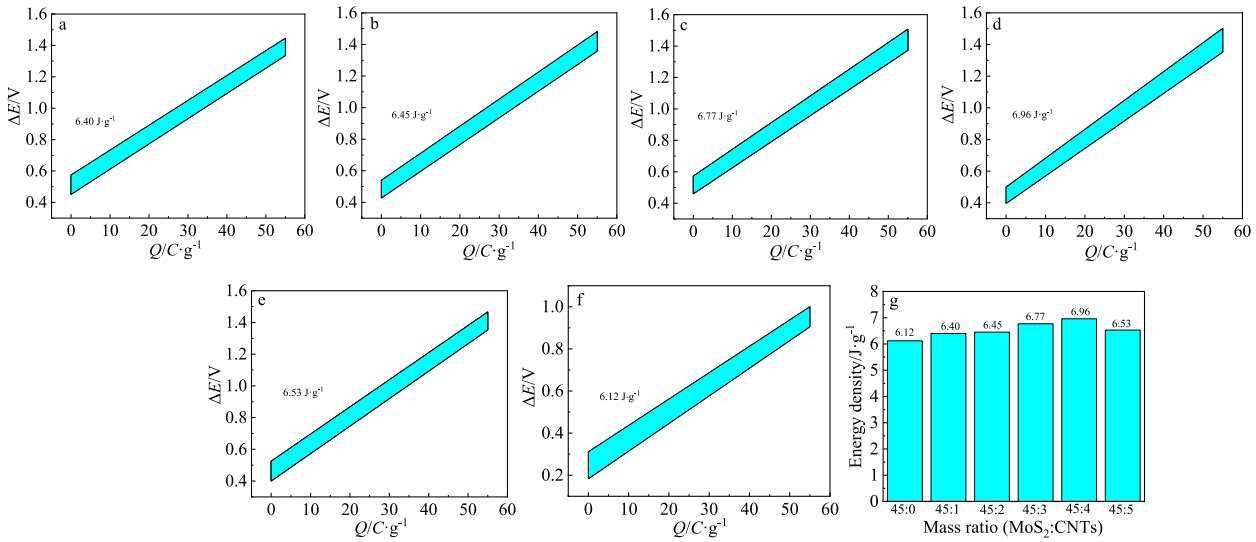

Fig. 13. Performance analysis results of extracting salinity gradient energy. (a–e) Salinity gradient energy extracted from a salt difference capacitor consisted of MoS_2/MWCNTs composite electrode with the mass ratio of 45:1 to 45:5 and AC electrode under a complete cycle; (f) Salinity gradient energy extracted of pure MoS_2 under a complete cycle; (g) Bar graphs of extracted salinity gradient energy with the mass ratio ranging from 45:1 to 45:5.

Compared with the previous reports of 38.2 mJ·cm^{-2} by F. Mantia [34]et al. , 13 mJ·cm^{-2} by Lee J. [47] et al. , and 5.31 J·g^{-1} by X. Zhou [25] et al., the salinity gradient extracted in a complete cycle can be greatly improved, indicating that this material has promising applications in utilizing salt difference for power generation and contributes to the future development of sustainable energy.

4. Conclusions

In this work, we used a hydrothermal method to incorporate MWCNTs with MoS_2 to form MoS_2/MWCNTs composite material, which is further used as the anode for salt difference cell, forming a new type of salt difference cell. Compared to pure molybdenum disulfide, both the electrochemical performance of the electrode itself and the salinity gradient energy extracted by the salt difference cell composed of AC as the cathode were greatly improved. The energy density extracted in a complete cycle reached 6.96 J·g^{-1}, which is 13.7% improvement. We demonstrated that the MoS_2/MWCNTs composite materials exhibited good performance in salt differential energy extraction, showing promising application prospects. However, the issue of cycle performance deviation still needs to be addressed.

Acknowledgements

This research work was financially supported by the Tianfu Emei Plan of Sichuan Province of the People's Republic of China (No. 1942).

References

[1] Ball P. A pinch of salt[J]. Nat. Mater., 2011, 10(5): 344. 344.
[2] Nijmeijer K, Metz S. Chapter 5 salinity gradient energy[J]. Sustain. Sci. Eng., 2010, 2(9): 95–139.
[3] Straub A P, Deshmukh A. Pressure-retarded osmosis for power generation from salinity gradients: is it viable?[J]. Energy Environ. Sci., 2016, 9(1): 31–48.
[4] Klaysom C, Cath T Y, Depuydt T. Forward and pressure retarded osmosis: potential solutions for global challenges in energy and water supply[J]. Chem. Soc. Rev., 2013, 42(16): 6959–6989.
[5] Skilhagen S E, Dugstad J E, Aaberg R J. Osmotic power — power production based on the osmotic pressure difference between waters with varying salt gradients[J]. Desalination, 2008, 220(1–3): 476–482.
[6] Thorsem T, Holt T. The potential for power production from salinity gradients by pressure retarded osmosis[J]. J. Membr. Sci., 2009, 335(1–2): 103–110.
[7] Logan B E, Elimelech M. Membrane-based processes for sustainable power generation using water[J]. Nature, 2012, 488(7411): 313–319.
[8] Yip N Y, Elimelech M. Comparison of energy efficiency and power density in pressure retarded osmosis and reverse electrodialysis[J]. Environ. Sci. Technol., 2014, 48(18): 11002–11012.
[9] Yip N Y, Tiraferri A, Phillip W A, Schiffma J D, Hoover L A, Kim Y C, Elimelech M. Thin-film composite pressure retarded osmosis membranes for sustainable power generation from salinity gradients[J]. Environ. Sci. Technol., 2011, 45(10): 4360–4369.
[10] Straub A P, Yip N Y, Elimelech M. Raising the bar: Increased hydraulic pressure allows unprecedented high power densities in pressure-retarded osmosis[J]. Environ. Sci. Technol. Lett., 2013, 1(1): 55–59.
[11] Tedesco M, Cipollina A, Tamburini A, Micale G. Towards 1 kW power production in a reverse electrodialysis pilot plant with saline waters and concentrated brines[J]. J. Membr. Sci., 2017, 522: 226–236.

[12] Lacey R E. Energy by reverse electrodialysis [J]. Ocean Eng., 1980, 7(1): 1−47.
[13] Post J W, Hamelers H VM, Buisman C JN. Energy recovery from controlled mixing salt and fresh water with a reverse electrodialysis system[J]. Environ. Sci. Technol., 2008, 42(15): 5785−5799.
[14] Post J W. Blue energy: electricity production from salinity gradients by reverse electrodialysis[D]. Netherlands: Wur Wageningen Ur, 2009.
[15] Veerman J, Saakes M, Metz S J, Harmsen G J. Reverse electrodialysis: Performance of a stack with 50 cells on the mixing of sea and river water[J]. J. Membr. Sci., 2009, 327(1−2): 136−144.
[16] Vermaas D A, Guler E, Saakes M. Theoretical power density from salinity gradients using reverse electrodialysis [J]. Energy Proc., 2012, 20(5): 170−184.
[17] Vermaas D A, Veerman J, Yip N Y, Elimelech M, Saakes M, Nijmeijer K. High efficiency in energy generation from salinity gradients with reverse electrodialysis[J]. ACS Sustain. Chem. Eng., 2013, 1(10): 1295−1302.
[18] Jung D H, Han E D, Kim B H, Seo Y H. Ultra-thin ion exchange film on the ceramic supporter for output power improvement of reverse electrodialysis[J]. Sci. Rep., 2019, 9(1): 17440−17459.
[19] Xin W W, Zhang Z, Huang X D, Hu Y H, Zhou T, Zhu C C, Kong X Y, Jiang L, Wen L P. High-performance silk-based hybrid membranes employed for osmotic energy conversion[J]. Nat. Commun., 2019, 10(1): 3876−3885.
[20] Tan G C, Zhu X P. Polyelectrolyte-coated copper hexacyanoferrate and bismuth oxychloride electrodes for efficient salinity gradient energy recovery in capacitive mixing [J]. Energy Technol., 2019, 8(1): 1900863−1900871.
[21] Zhou S, Xie L, Li X F, Huang Y A, Zhang L P, Lian Q R, Yan M, Zeng J, Qiu B L, Liu T Y, Tang J Y, Wen L P, Jiang L, Kong B. Interfacial super-assembly of ordered mesoporous carbon-silica/AAO hybrid membrane with enhanced permselectivity for temperature- and pH- sensitive smart ion transport[J]. Angew. Chem., Int. Ed., 2021, 60(50): 26167−26176.
[22] Shan Z, Xin Z, Lei X, Yan J H, Miao Y, Tian Y L, Hui Z, Lei J, Biao K. Dual-functional super-assembled mesoporous carbon-titania/AAO hetero-channels for bidirectionally photo-regulated ion transport[J]. Small, 2023, 19(32): 202301038−202301049.
[23] Rica R, Ziano R, Salerno D, Mantegazza F, Van R R, Brogioli D. Capacitive mixing for harvesting the free energy of solutions at different concentrations[J]. Entropy, 2013, 15(12): 1388−1407.
[24] Marino M, Misuri L, Jiménez M L, Ahualli S, Kozynchenko O, Tennison S, Brogioli D. Modification of the surface of activated carbon electrodes for capacitive mixing energy extraction from salinity differences[J]. J. Colloid Interface Sci., 2014, 436: 146−153.
[25] Zhou X, Zhang W B, Li J J, Bao X, Han X F, Thenint M M, Ma X J. An electrochemical system for salinity gradient energy harvesting[J]. Energy Convers. Manag., 2022, 255: 115315−115321.
[26] Brogioli D, Ziano R, Rica R A, Salerno D, Kozynchenko O, Hamelers H VM, Mantegazza F. Exploiting the spontaneous potential of the electrodes used in the capacitive mixing technique for the extraction of energy from salinity difference[J]. Energy Environ. Sci., 2012, 5(12): 9870−9880.
[27] Zhan F, Wang G, Wu T T, Dong Q, Meng Y L, Wang J R, Yang J, Li S F, Qiu J S. High performance asymmetric capacitive mixing with oppositely charged carbon electrodes for energy production from salinity differences[J]. J. Mater. Chem. A, 2017, 5(38): 20374−20380.
[28] Marino M, Kozynchenko O, Tennison S, Brogioli D. Capacitive mixing with electrodes of the same kind for energy production from salinity differences[J]. J. Phys.-Condes. Matter, 2016, 28(11): 114004−114013.
[29] Balzer C, Qing L, Wang Z G. Preferential ion adsorption in blue energy applications[J]. ACS Sustain. Chem. Eng., 2021, 9(28): 9230−9239.
[30] Brogioli D. Extracting renewable energy from a salinity difference using a capacitor [J]. Phys. Rev. Lett., 2009, 103(5): 58501−58504.
[31] Ahualli S, Fernández M M, Iglesias G, Delgado Á V, Jiménez M L. Temperature effects on energy production by salinity exchange[J]. Environ. Sci. Technol., 2014, 48(20): 12378−12385.
[32] Sales B B, Saakes M, Post J W, Buisman C JN, Biesheuvel P M, Hamelers H VM. Direct power production from a water salinity difference in a membrane-modified supercapacitor flow cell[J]. Environ. Sci. Technol., 2010, 44(14): 5661−5665.
[33] Liu F, Schaetzle O, Sales B B, Saakes M, Buisman C JN, Hamelers H VM. Effect of additional charging and current density on the performance of Capacitive energy extraction based on Donnan Potential[J]. Energy Environ. Sci., 2012, 5(9): 8642−8650.
[34] La M F, Pasta M, Deshazer H D, Logan B E, Cui Y. Batteries for efficient energy extraction from a water salinity difference[J]. Nano Lett., 2011, 11(4): 1810−1813.
[35] Ye M, Pasta M, Xie X, Dubrawski K L, Xu J, Liu C, Criddle C S. Charge-free mixing entropy battery enabled by low-cost electrode materials[J]. ACS Omega, 2019, 4(7): 11785−11790.
[36] Ye M, Pasta M, Xie X, Cui Y, Criddle C S. Performance of a mixing entropy battery alternately flushed with wastewater effluent and seawater for recovery of salinity-gradient energy[J]. Energy Environ. Sci., 2014, 7(7): 2295−2300.
[37] Zhou S, Xie L, Zhang X, Yan M, Zeng H, Liang K, Jiang L, Kong B. Super-assembled multi-level asymmetric mesochannels for coupled accelerated dual-ion selective transport[J]. Adv. Mater., 2022, 35(7): 2208903−2208913.
[38] Shi Y B, Pu J B, Wang L P. Structural phase transformation in amorphous molybdenum disulfide during friction[J]. J. Phys. Chem. C, 2020, 125(1): 836−844.
[39] Li X L, Li T C, Huang S, Zhang J, Pam M E, Yang H Y. Controllable synthesis of two-dimensional molybdenum disulfide (MoS_2) for energy-storage applications[J]. ChemSusChem, 2020, 13(6): 1379−1391.
[40] Guo W, Li X R, Cui L, Li Y F, Zhang H, Ni T J. Promoting the anode performance of microbial fuel cells with nano-molybdenum disulfide/carbon nanotubes composite catalyst[J]. Bioproc. Biosyst. Eng., 2021, 45(1): 159−170.
[41] Shuai J, Yoo H D, Liang Y, Li Y, Yao Y, Grabow L C. Density functional theory study of Li, Na, and Mg intercalation and diffusion in MoS_2 with controlled interlayer spacing[J]. Mater. Res. Express, 2016, 3(6): 64001−64006.
[42] Li J J, Zhang W B, Zhou X, Theinet M M, Yin Y, Yang J L, Yang Z Q, Ma X J. Electrochemical conversion of salinity gradient energy via molybdenum disulfide electrode[J]. J. Electrochem. Soc., 2023, 170(2): 20518−20524.
[43] Wang C H, Zhang Y F. Preparation of molybdenum disulfide/graphene composite electrode and its electrochemical sodium storage performance[J]. Mod. Chem. Ind., 2020, 40(4): 158−166.
[44] Diulus J T, Elzein R, Addou R, Herman G S. Surface chemistry of 2-propanol and O_2 mixtures on SnO_2(110) studied with ambient-pressure x-ray photoelectron spectroscopy[J]. J. Chem. Phys., 2020, 152(5): 54713−54721.

[45] Zhu H, Lai J, Arges C G, Wang Y, Zhu X. Engineering the interlayer spacing of molybdenum disulfide for efficient salinity gradient energy recovery in concentration flow cells [J]. Electrochim. Acta, 2020, 342(8): 136103−136110.
[46] Yoo H D, Li Y, Liang Y, Lan Y, Wang F, Yao Y. Intercalation pseudocapacitance of exfoliated molybdenum disulfide for ultrafast energy storage[J]. ChemNanoMat, 2016, 2(7): 688−691.
[47] Lee J, Yoon H, Lee J, Kim T, Yoon J. Corrigendum: Extraction of salinity-gradient energy by a hybrid capacitive-mixing system[J]. ChemSusChem, 2018, 11(3). 638−638.

二硫化钼和碳纳米管复合物电极用于盐差能转换

李家俊，张伟彬*，刘鑫宇，杨静蕾，尹易，杨泽钦，马雪婧*
成都理工大学材料与化学化工学院，四川 成都 610059

摘要

海洋占地球水资源总量的 97%，地表面积的 70%以上。随着化石燃料等不可再生能源的持续消耗与可再生能源的快速发展，人们对海洋资源的利用越来越重视。海洋能包括潮汐能、波浪能、温差能和盐差能等。其中盐差能是海水和淡水相互作用产生的能量，是以化学能形式存在的海洋能，这种能量较多产生在河口处。目前，压力延迟渗透技术、反电渗析技术和电容混合技术是转换盐差能的三种主要技术。本文构建了一种基于电容混合技术的新型盐差电池，使用二硫化钼和多壁碳纳米管复合物电极作为阳极，活性炭作为阴极。将两种不同离子储存机制的材料复合在一起，二硫化钼具有类似石墨烯的层状结构，层间间距约为石墨烯的两倍，是一种可以与钠离子发生插层反应的电池电极材料。多壁碳纳米管具有典型的双电层效应，放电时在其表面吸附钠离子的同时，可以帮助钠离子更快地进入二硫化钼层间，加快离子传输效率和盐差能的转换效率。对该复合材料进行物理和电化学表征，并与活性炭电极组装的盐差电池，测试其盐差能转换能力。浓度响应电压 150 mV，经过一个完整的四步循环后，转换能量密度可达 6.96 $J \cdot g^{-1}$。该器件原材料价格较低，并且不使用离子膜，更加环保，为转换盐差能的研究提供了一种新途径。

关键词：盐差量；电化学转化；转换效率；二硫化钼；碳纳米管